Geophysical Research Letters

RESEARCH LETTER
10.1029/2020GL087508

Rupture Dynamics of the 2012 Nicoya M_w 7.6 Earthquake: Evidence for Low Strength on the Megathrust

Suli Yao[1] and **Hongfeng Yang**[1]

[1]Earth System Science Programme, The Chinese University of Hong Kong, Shatin, Hong Kong

Key Points:
- We resolve the dynamic rupture process of the 2012 Nicoya M_w 7.6 earthquake with constraints from near-field observations
- The preferred dynamic rupture model shows remarkable fit on near-field displacements and velocity waveforms
- Strength on Nicoya megathrust prior to the earthquake is inferred to be very low (~7.5 MPa), indicating the near-lithostatic pore pressure

Supporting Information:
- Supporting Information S1

Correspondence to:
H. Yang,
hyang@cuhk.edu.hk

Citation:
Yao, S., & Yang, H. (2020). Rupture dynamics of the 2012 Nicoya M_w 7.6 earthquake: Evidence for low strength on the Megathrust. *Geophysical Research Letters*, *47*, e2020GL087508. https://doi.org/10.1029/2020GL087508

Received 15 FEB 2020
Accepted 5 JUN 2020
Accepted article online 9 JUN 2020

Abstract Frictional properties on subduction interfaces are essential for understanding earthquake nucleation, rupture propagation, and tsunami generation during megathrust earthquakes. Because they cannot be directly observed, they have been inferred from different approaches. However, none of them have reported constraints immediately before a megathrust earthquake. Here we quantify the frictional strength on the megathrust prior to the 2012 M_w 7.6 Nicoya earthquake by conducting spontaneous rupture simulations with constraints from near-field observations. Our preferred dynamic rupture model shows a remarkable fit on the near-field data. The simulation results indicate an average strength drop of <5 MPa. Considering typical ranges for the dynamic friction coefficient $f_d \leq 0.2$ and the static friction coefficient $f_s = 0.6$, we infer that the average strength on the megathrust is ≤7.5 MPa. Such low strength is attributed to the near-lithostatic pore pressure along the subduction interface, which is implied by seismic studies in this region.

Plain Language Summary Subduction zones host a preponderance of great earthquakes that are sometimes accompanied by destructive tsunamis. The frictional resistance (strength) on subduction interfaces, termed *megathrusts*, plays critical roles in controlling earthquake rupture process and thus significantly impacts the ground motion intensity and the tsunamigenic potential during earthquakes. However, the strength on the megathrust is difficult to estimate directly and evolves over time. Here, we constrain the strength on the Nicoya megathrust shortly before the 2012 Nicoya M_w 7.6 earthquake with constraints from near-field observations. Based on the simulation results, we infer the strength on the megathrust prior to the earthquake to be less than 7.5 MPa. Such low strength at ~25 km in depth indicates the existence of compacted fluids with a high pore pressure.

1. Introduction

Faults slip when shear stress (τ_0) exceeds yield stress (τ_s), the static frictional resistance, generating a variety of slip modes such as earthquakes, slow slip events (SSEs), and creeping. However, both the stress level and the yield stress on natural faults remain elusive due in part to the lack of direct measurements, although they are well known to play critical roles in earthquake generation and seismic radiation during dynamic ruptures (Dunham, 2007; Harris, 2004; Weng et al., 2015). Multiple lines of evidences suggest that the strength is low in regions of aseismic slip. For instance, rate-state numerical simulations suggest an extremely low (<2 MPa) strength in the source region of SSEs downdip to the locked megathrust to match their recurrence intervals (Liu & Rice, 2007). Furthermore, the static friction coefficient derived from laboratory experiments on fault gouge samples from the shallow creeping section of the San Andreas Fault is ~0.2 owing to the presence of smectite clay minerals (Carpenter et al., 2011; Lockner et al., 2011), significantly lower than 0.6 that was commonly obtained for most materials (Byerlee, 1978). The strength on seismogenic faults is not a constant but features instability during earthquakes. Fault strength drastically drops from the yield stress (τ_s) to a low dynamic stress (τ_d) with a friction coefficient of <0.2 (Di Toro et al., 2011). Such low coseismic resistances have been confirmed by postseismic temperature measurements on seismogenic faults (Fulton et al., 2013; Kano et al., 2006; Li et al., 2015). Furthermore, heat flow measurements imply low long-term average frictional resistances on seismogenic faults over multiple earthquake cycles (Gao & Wang, 2014; Lachenbruch & Sass, 1980). However, due to the lack of constraints on the strength evolution, the yield stress on faults prior to ruptures remains poorly understood.

In addition to the strength, the shear stress on megathrusts remains elusive and by far is indirectly derived and suggested to be low from different approaches. Studies of stress field modeling in forearcs with

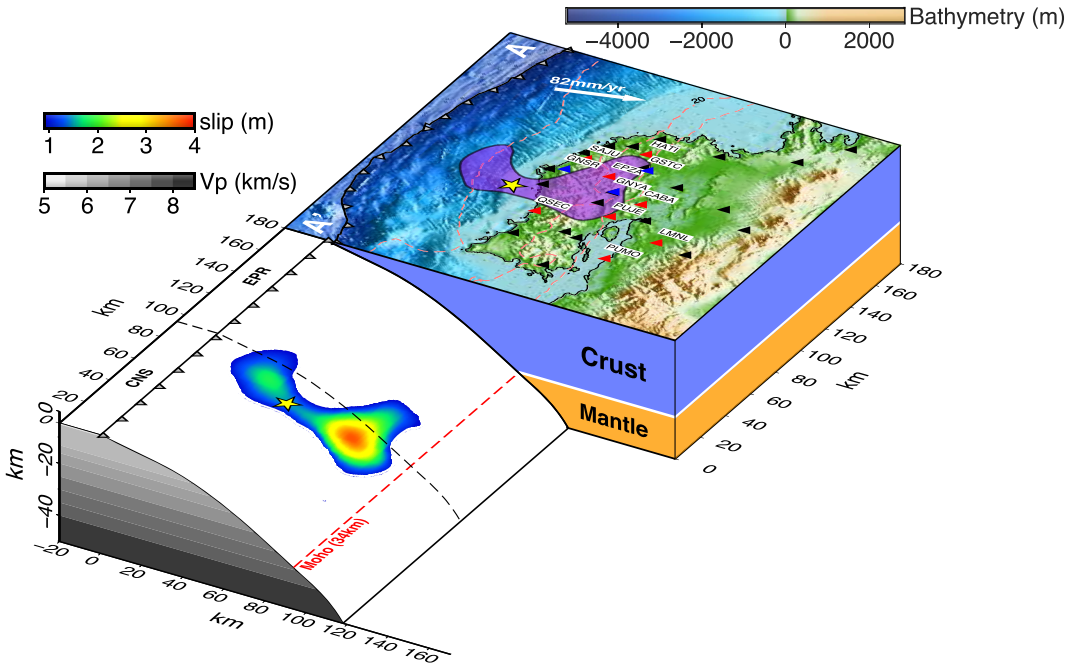

Figure 1. A 3-D model for the study region. Upper block: The purple area is the projection of the ruptured patch with slip over 1 m (Yue et al., 2013). The yellow star is the epicenter. Red, black, and blue triangles are continuous GPS, campaign GPS, and strong motion stations, respectively. Light red dashed lines represent slab depths of 10, 20, and 30 km. Bottom block: Slip distribution in Yue's model. The yellow star denotes the hypocenter. The red dashed line denotes the depth of Moho. The black dashed line is the boundary between the oceanic crusts originated from Cocos-Nazca spreading center (CNS) and East Pacific Rise (EPR).

constraints from stress orientation observations (Seno, 2009), the force balance for mountain building (Lamb, 2006), or the stress field rotation across a megathrust (Li et al., 2018) commonly suggest a low mean shear stress on megathrusts (<50 MPa). Hardebeck (2015) has found that most megathrusts are nonoptimally oriented with angles of 45°–60° between the maximum compressive stress and the subduction interface, indicating a low stress environment on megathrusts. Similarly, analyses of coseismic stress rotations suggest that prestress levels are on the order of stress drops in several megathrust earthquakes such as the 2011 Tohoku M_w 9.0 and the 2010 Maule M_w 8.8 earthquakes (Hardebeck, 2012). Yield stress serves as the upper bound for shear stress during interseismic periods. However, the difference between the yield stress and the shear stress (strength excess) preceding earthquakes has been poorly constrained.

Estimates of the strength excess and the strength drop, the difference between the yield stress and the dynamic frictional resistance, require solving the dynamic rupture process. Therefore, dynamic inversions with constraints from near-field observations have been conducted (Gallovič et al., 2019; Ma et al., 2008; Weng & Yang, 2018). However, megathrust earthquakes usually do not have very good near-field constraints due to the offshore locations, leading to ambiguities in dynamic rupture models. Here we investigate the strength on the megathrust in the Nicoya Peninsula region, where the Cocos plate subducts beneath the Caribbean plate with an average convergence rate of 82 mm/year (DeMets et al., 2010), characterized by M 7.5 + megathrust earthquakes with time intervals of 50–60 years (Protti et al., 2001). The latest event happened in 2012 with a moment magnitude of 7.6 (Figure 1). Dynamic rupture scenarios derived from interseismic locking models (Yang et al., 2019) match the first-order source parameters in the kinematic models, such as the moment magnitude and the rupture extent. However, these scenarios do not have constraints on stress and strength on the megathrust (Yang et al., 2019). Because the Nicoya Peninsula sits right over the major ruptured patch of the megathrust, land-based observations provide unique opportunities in monitoring slip behaviors and resolving physical properties on the megathrust. We utilize near-field observations to constrain the strength prior to the 2012 M_w 7.6 earthquake by dynamic rupture simulations.

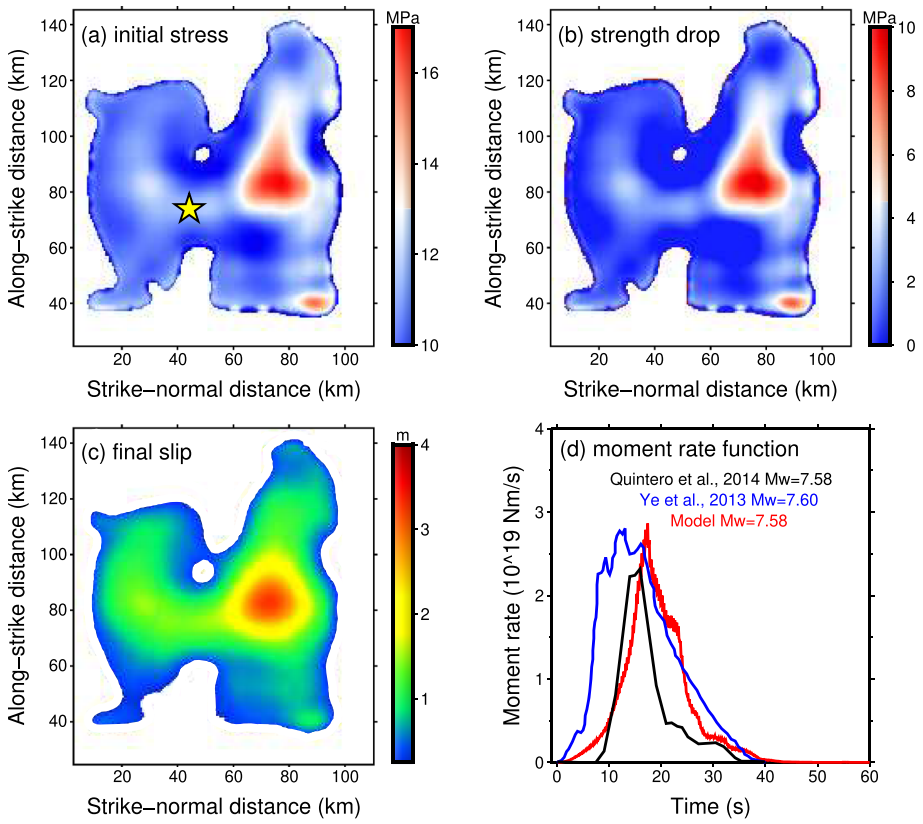

Figure 2. Parameters in the preferred dynamic rupture model: (a) initial stress distribution and hypocenter (star), (b) strength drop, (c) final slip distribution, and (d) moment rate functions of our result (red) and two kinematic source models (black and blue).

2. Method and Model Setup

We conduct dynamic rupture simulations on a 3-D cubic elastic model with an embedded curved megathrust. The elastic model extends 180 km along strike, 190 km strike-normal, and 70 km in depth, sufficiently large to avoid boundary effects. Fault parameterization and material properties are consistent with the settings in the finite fault kinematic model of the 2012 Nicoya M_w 7.6 earthquake (Yue et al., 2013): The strike angle is set to be 307°; the 2-D fault geometry is defined according to a seismic reflection profile (Christeson et al., 1999); and a 1-D depth-dependent layered velocity model is adopted (Audet & Schwartz, 2013) (Table S1).

In order to meet numerical requirements to resolve the rupture front, the cohesive zone, where the stress decreases from the static to dynamic level, must be 3 to 5 times larger than the grid size on faults (Day et al., 2005). We thus set the grid size on the fault to be 250 m (see details in the supporting information). A time step of 0.007 s is adopted in simulations. The grid size on the ground surface increases from 250 m near the trench to 3 km on the boundaries. Most near-field stations correspond to surface grids of ~1 km. We test the effects of the surface grid size on synthetic ground velocities by comparing their results with results from the uniform surface grid size of 500 m. Synthetic waveforms in the two models are nearly identical (Figure S3).

We adopt a linear slip-weakening (LSW) law (Ida, 1972) on the fault, in which the frictional resistance (τ_f) decreases linearly from the yield stress (τ_s) to the dynamic stress (τ_d) with slip (δ) over a critical weakening distance (D_0) (Equation 1). Rupture propagation is controlled by the strength excess ($\tau_s - \tau_i$), strength drop ($\tau_s - \tau_d$), and D_0, which are represented by three free parameters (B, S, and C) in our models and will be constrained by a grid search. We initially assume a constant effective normal stress (σ_n) on the megathrust (i.e., 50 MPa), which determines the values of τ_s and τ_d after the selection of static (f_s) and dynamic (f_d)

friction coefficients (Equations 4 and 5). Because we can only constrain the strength drop ($\tau_s - \tau_d$), the initial value of σ_n does not matter, as it is coupled with the difference between the static and dynamic friction coefficients. How to separate them will be discussed later.

We first calculate the static stress drop ($\Delta\tau_{kin}$) from a kinematic slip model of the 2012 Nicoya earthquake (Yue et al., 2013). Assuming a uniform dynamic stress (i.e., 10 MPa), we can then estimate the initial stress τ_i (Figure 2a), which is the summation of the static stress drop and the dynamic stress (Yang et al., 2019). To account for the potential overshoot or undershoot process during the rupture, we introduce a free parameter B to multiply the static stress drop (Equation 2) and search for the best fit value of B, which is constrained to be 0.8 based on the misfit patterns for coseismic static displacements and the moment magnitude of the Nicoya earthquake (Figure S4; see details in the supporting information).

It is well known that there is an intrinsic trade-off between the strength drop and D_0 (Guatteri & Spudich, 2000). By utilizing different source parameters, e.g., rupture speed and slip distribution, the trade-off can be removed because the trade-off trend for each parameter differs from each other (Weng & Yang, 2018). D_0 is suggested to scale with the final slip distribution (Rice, 2006; Viesca & Garagash, 2015) and thus is heterogeneous (Equation 3). We also compare the case with a uniform distribution of D_0 with the average value in a range of 0.2–0.6 m. The strength drop ($\tau_s - \tau_d$) is controlled by the seismic ratio S (Equation 4). In areas with slip smaller than the cutoff value (i.e., 0.3 m), the strength (τ_s) is artificially prescribed to be high (i.e., 25 MPa) to stop ruptures. We utilize an open-source finite-element package, PyLith (Aagaard et al., 2013), to run simulations.

$$\tau_f(\delta) = \begin{cases} \tau_s - \dfrac{\delta}{D_0} \times (\tau_s - \tau_d) & \delta < D_0 \\ \tau_d & \delta \geq D_0 \end{cases} \tag{1}$$

$$\vec{\tau_i} = \vec{\tau_d} + B * \overrightarrow{\Delta\tau_{kin}} \tag{2}$$

$$D_0 = C * u_{kin} \tag{3}$$

$$\tau_s = f_s \times \sigma_n = (1 + S) * \left(\left|\vec{\tau_i}\right| - \left|\vec{\tau_d}\right|\right) + \left|\vec{\tau_d}\right| \tag{4}$$

$$\tau_d = f_d \times \sigma_n \tag{5}$$

Ruptures are nucleated from the hypocenter at 9.76°N, 85.56°W, and 13 km in depth. To minimize the artificial effects, we nucleate ruptures by a time-weakening scenario with a constant rupture speed of 1.6 km/s, which spontaneously transforms into the slip-weakening mechanism. The prescribed initial rupture speed only impacts the early stage of rupture propagation, while its effect on later stages that dominate the energy is negligible (Figure S5). Ruptures stop spontaneously before reaching the strength barrier when the strength or D_0 exceeds critical values, termed *self-arresting ruptures*, due to the insufficient energy to overcome the fracture energy on the fault (Weng & Yang, 2017). Contrarily, some ruptures eventually break both the offshore and onshore patches, classified as breakaway ruptures. The boundaries between the two types of ruptures in the parameter domain are denoted by self-arresting lines (Figure 3).

3. Constraints on Strength Drop in Dynamic Simulations From Near-Field GPS Data

We calculate the standard misfits between synthetics and vertical velocity waveforms at six high-rate GPS stations and three strong motion stations for all breakaway ruptures (Figure 3). Due to the significant amplification effects on the high-rate GPS stations LMNL and PUMO, we exclude the two stations from the misfit calculation (see details in the supporting information). We apply a band-pass filter of 0.02–0.25 Hz on both data and synthetic waveforms, slightly higher than the high-frequency end (i.e., 0.2 Hz) in the kinematic source model (Yue et al., 2013). Then we calculate the least squares misfits for waveforms in a 20-s window, centered at the peak velocities. Considering the possible biases in picking arrivals, the imperfect velocity structure, and the effects of the artificial nucleation process, synthetic waveforms are allowed to shift in ±2 s windows to search for the minimum of misfit. Allowing shift in ±1 s windows results in similar misfit

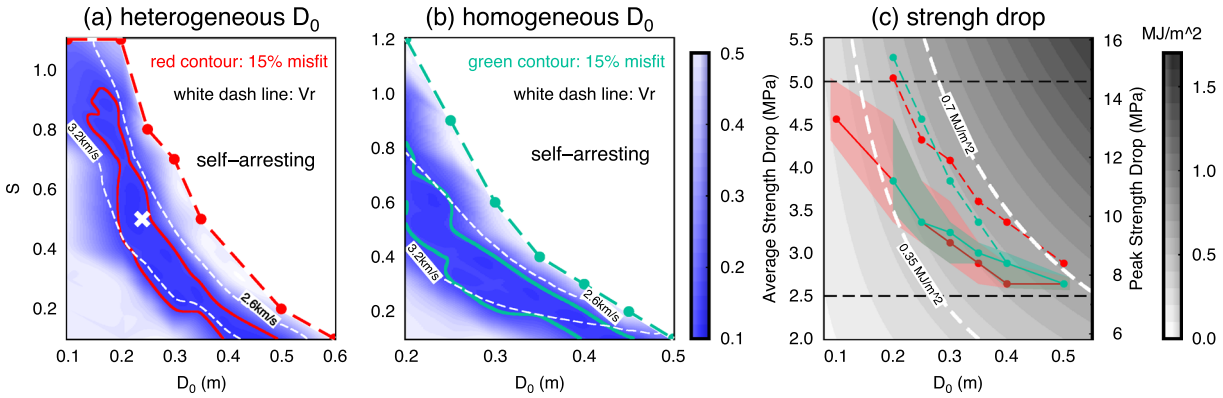

Figure 3. Misfits in velocity waveforms using a (a) heterogeneous and (b) uniform distribution of D_0. Colored solid lines indicate the contours with misfit less than 15% (red in (a) and green in (b)). Colored dashed lines represent the boundaries between breakaway and self-arresting ruptures. White dashed lines denote rupture speeds of 2.6 and 3.2 km/s, respectively. The white cross in (a) denotes the preferred model with the minimum misfit. (c) Grayscale colors represent the fracture energy associated with different parameters. Red and green dashed lines with dots correspond to self-arresting lines with heterogeneous and uniform distribution of D_0, respectively. Solid dotted lines show the best fit parameter groups, with 15% misfit shown in shadow.

patterns (Figure S7). Then we take the average among the nine stations as the misfit in velocity waveform for each model.

The minimum of the waveform misfit is around 10%, yielding an average D_0 value of ~0.25 m (Figure 3a). There is still a slight trade-off with the strength drop (Figure 3a). The area with a misfit of <15% coincides with the area between contours of rupture speed in 2.6–3.2 km/s. We also compare the cases with uniform distribution of D_0, whose results are similar in the trade-off trend (Figure 3b). The best fit value of D_0 (0.25 m) is identical to the value assuming a slip-scaled D_0. Then we inspect the modeled rupture process with the best fit solution of frictional parameters (white cross in Figure 3a). The rupture front propagates both downdip and updip, then reaches the downdip limit at ~20 s and starts to propagate along strike, and eventually terminates at ~40 s (Figures S8 and S9). The total moment released in the best fit scenario is 2.97×10^{20} N m, equivalent to a moment magnitude of 7.58, well consistent with observations. The peak slip is 3.6 m on the downdip patch (Figure 2c). The moment rate function is consistent in duration, shape, and the peak value with kinematic source models (Figure 2d). Moreover, the synthetic surface responses remarkably fit the near-field displacements and velocities (Figure 4), except the horizontal components of the station GNSR. We find that the horizontal ground motions at GNSR were not well resolved in long periods. Overall, the great coherence between synthetics and data indicates the reliability of our preferred dynamic rupture model.

The best fit average value of D_0 is 0.25 m, corresponding to a S ratio of 0.5. Thus, the strength drop is 3.6 MPa. If we consider the trade-off trend and take the average value of D_0 from 0.2 to 0.6 m, the average strength drop is constrained to be $\leq$5 MPa with a peak value of $\leq$12 MPa on the downdip patch (Figure 3c). According to the self-arresting lines, the upper bound for the strength drop in breakaway cases is 15 MPa. The average fracture energy on the ruptured fault is constrained to be 0.35–0.7 MJ/m^2.

We test the dependences of dynamic rupture simulations on the kinematic model. We apply the same parameter group (C0.125, B0.8, and S0.5) in the preferred model and follow the same procedure to conduct dynamic rupture simulations based on the other kinematic model (Liu et al., 2015), which differs with Yue's model by using a planar fault model and more near-field GPS data. The dynamic model derived from Liu's kinematic model has a similar final slip pattern and a nearly identical moment magnitude with that derived from Yue's model (Figures S10 and S11). Synthetic waveforms in this dynamic model have a comparable fit on near-field data with that derived from Yue's kinematic model (Figures 4 and S11), demonstrating that our determination of frictional properties is robust and independent on kinematic models.

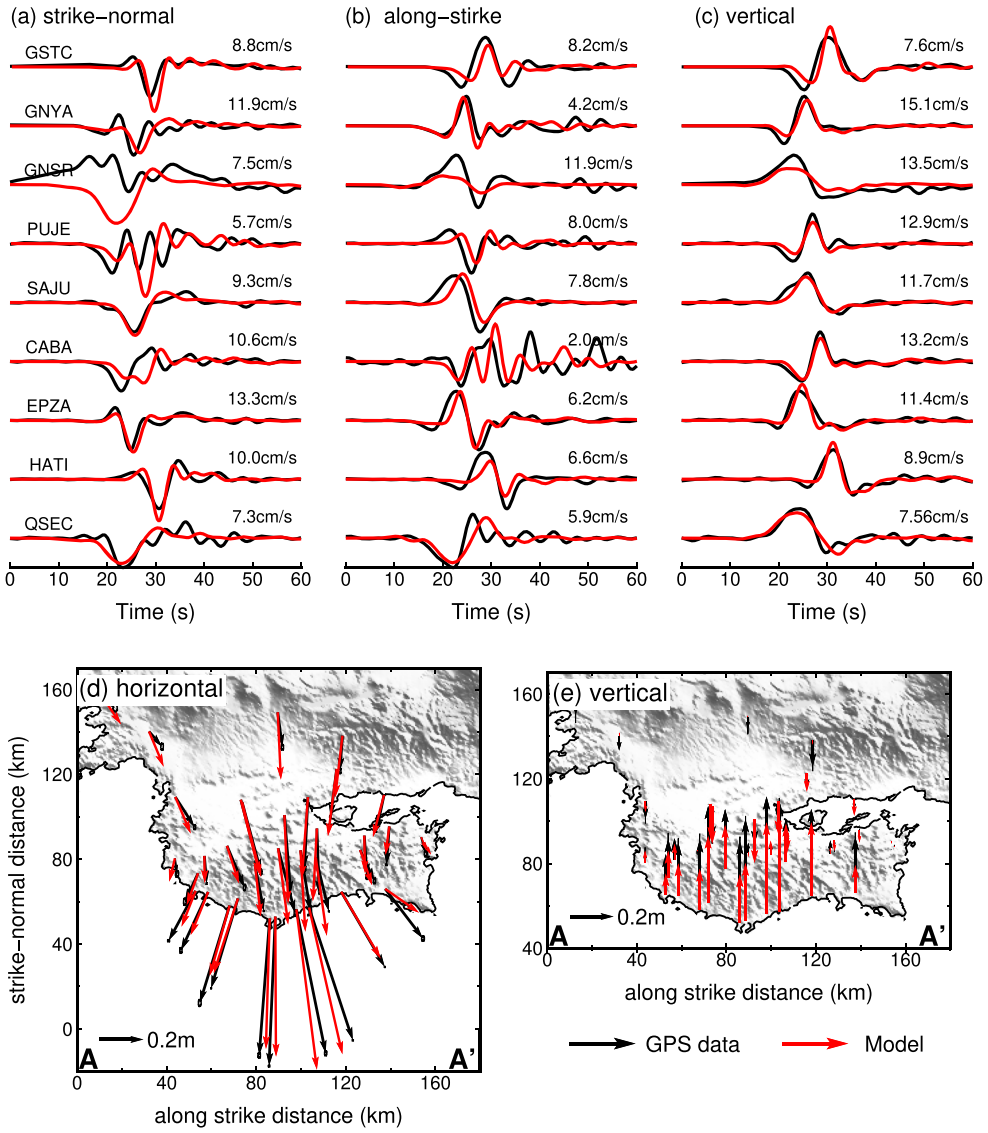

Figure 4. Data on high-rate GPS and strong motion stations (black) and synthetics from the best fit model (red) in three directions: (a) strike-normal, (b) along strike, and (c) vertical. Station locations are in Figure 1. Numbers on the top of each trace are the peak ground velocities from measurements. Measured (black) and computed (red) static coseismic displacements in (d) horizontal and (e) vertical directions.

4. Estimates of the Effective Normal Stress and Yield Stress on the Nicoya Megathrust

The yield stress on the megathrust is the product of the effective normal stress (σ_n) and the static friction coefficient ($\tau_s = \sigma_n \times f_s$), where the effective normal stress is the difference between normal stress and pore pressure ($\sigma_n = \sigma - P$). According to laboratory experiments, the typical value of the static friction coefficient is ~0.6 for various types of rocks and fault gouges (Byerlee, 1978; Di Toro et al., 2011; Kuo et al., 2013; Yao et al., 2013). The dynamic friction coefficient on natural faults has been estimated to be extremely low (0.04–0.08) during earthquakes, based on postseismic in situ temperature measurements such as the 2011 Tohoku earthquake (with a residual stress of 0.54 MPa; Fulton et al., 2013) and the 1999 Chi-Chi earthquake (0.7–1.7 MPa; Kano et al., 2006). However, such drilling projects are expensive and hence cannot be universally employed. In laboratory experiments, a significant drop in friction coefficient from f_s to f_d during fast sliding has been identified and attributed to various physicochemical processes such as flash heating on

contact asperities, thermal decomposition, and melting, termed *fault lubrication phenomena* (Di Toro et al., 2011).

Although pervasive weakening has been observed, different values of f_d have been reported from experiments on different rock samples. For instance, experiments on calcite usually maintain nearly complete strength drops with $f_d < 0.1$ (Han et al., 2007; Violay et al., 2015); while for basalt, f_d ranges from 0 to 0.3 under similar experimental settings (Violay et al., 2015). Experiments on fault gouges commonly report low f_d (0–0.3) (Di Toro et al., 2011; Kuo et al., 2013; Yao et al., 2013). Among experiments on various rock types, a general rule is that the magnitude of f_d is negatively correlated with the normal stress (σ_n) and the slip rate, as they control the heating process that drives various lubrication mechanisms. For instance, f_d for dolomite dry gouges decreases from 0.28 to 0.10 when σ_n increases from 0.43 to 2.04 MPa under the slip rate of 1.3 m/s and decreases from 0.41 to 0.21 when the slip rate increases from 0.693 to 1.3 m/s under a σ_n of 1.21 MPa (De Paola et al., 2011). We infer the range for f_d on the Nicoya megathrust based on experiment results with the following constraints: (1) given the estimated average strength drop of 5 MPa, we reasonably discard experiment results with σ_n under 5 MPa; and (2) we only refer to the experiment results with a slip rate of ~1 m/s, the typical seismic slip rate. As such, we take an upper bound of 0.2 for f_d, corresponding to our initially prescribed value of the dynamic stress.

If the pore pressure does not change during the coseismic slip, the coseismic strength drop can be calculated as $\tau_s - \tau_d = \sigma_n \times (f_s - f_d)$. Therefore, the effective normal stress is estimated as $\sigma_n = \frac{(\tau_s - \tau_d)}{(f_s - f_d)}$, inversely proportional to the reduction in friction coefficient and proportional to the strength drop. Based on our simulation results, the average strength drop ($\tau_s - \tau_d$) is constrained to be 2.5–5 MPa. To estimate the yield stress $\tau_s = \sigma_n \times f_s$, we adopt f_s to be 0.6 and $f_d \leq 0.2$. Given $f_s = 0.6$, $f_d = 0.2$, and an average strength drop of 5 MPa, we can derive the upper bounds for the average σ_n and τ_s to be 12.5 and 7.5 MPa, respectively, while the lower bounds for the average σ_n and τ_s are estimated to be 4.2 and 2.5 MPa, respectively, by giving $f_d = 0$ and an average strength drop of 2.5 MPa. Similarly, the peak σ_n and τ_s on the downdip patch are estimated to be 11.7–30 and 7–18 MPa, respectively, by considering the peak strength drop of 7–12 MPa.

However, the effective normal stress may not be a constant during the coseismic process, as the pore pressure has been suggested to change during earthquakes. Field observations suggest that most coseismic slip is accommodated in millimeter-thick shear zones adjacent to fault interfaces (Noda & Shimamoto, 2005; Tanikawa & Shimamoto, 2009), leading to a localized temperature rise up and a consequent increase in pore pressure. Experiments on field samples suggest low values for permeability in slip zones (10^{-19} m^2), 3 orders lower than the surrounding damage zones (10^{-16} m^2) (Noda & Shimamoto, 2005), forming an unfavorable condition for draining outward from slip zones. Therefore, coseismic draining is likely unable to eliminate the temperature-induced pore pressure rise up; hence, the coseismic pore pressure change should be positive. This phenomenon, termed *thermal pressurization*, has been adopted in numerical simulations (Noda & Shimamoto, 2005; Rice, 2006; Tanikawa & Shimamoto, 2009) to explain unexpected slip distribution in earthquakes such as the 1999 Chi-Chi M_w 7.6 and the 2011 Tohoku M_w 9.0 events (Tanikawa & Shimamoto, 2009; Ujiie et al., 2013).

When we consider a positive coseismic pore pressure change ($\Delta P > 0$), dynamic stress should be calculated as $\tau_d = (\sigma_n - \Delta P) \times f_d$; thus, the effective normal stress before the earthquake is calculated as $\sigma_n = \frac{\tau_s - \tau_d - \Delta P * f_d}{f_s - f_d}$. In the case with a positive ΔP, the yield stress and the effective normal stress are estimated to be lower than the case discussed above with a constant σ_n ($\Delta P = 0$). Here we suggest the upper bounds for the average σ_n and τ_s on the Nicoya megathrust to be 12.5 and 7.5 MPa, respectively, and the peak σ_n and τ_s to be lower than 30 and 18 MPa, respectively, on the down-dip patch.

5. The Spatial Pattern of Strength on the Nicoya Megathrust

Such low strength (i.e., 7.5 MPa on average) on the Nicoya megathrust is consistent with local seismic observations. It is well known that the strength is critical in controlling earthquake recurrence intervals (Liu & Rice, 2007; Matsuzawa et al., 2010; Yang et al., 2012). Numerical simulations of earthquake cycles

indicate a positive correlation between the recurrence interval and the effective normal stress (Kato, 2012). Given the observed relatively short earthquake intervals (50–60 years) in the Nicoya region, a low effective normal stress is anticipated. Before the 2012 earthquake, large SSEs had been reported to occur updip, downdip, and southeast of the locked-then-ruptured megathrust every 2–3 years (Dixon et al., 2014). According to numerical simulations (Liu & Rice, 2007), recurrence intervals of SSEs can be reached when the effective normal stress is ~4–7 MPa. As such, we propose a modest contrast in strength between the seismogenic zone (~10 MPa) and adjacent SSE zones (~2–4 MPa). Moreover, Walter et al. (2011) found tremors at the seismogenic depth within the rupture extent of the 2012 earthquake, indicating a heterogeneous strength distribution within the locked megathrust.

A near-lithostatic pore pressure can be deduced from the low strength on the Nicoya megathrust. Fluids in subduction zones may originate from the sediment dewatering process at shallow depths, as well as metamorphic dehydration reactions at greater depths. As an evidence of high fluid content, seismological studies have identified high *Vp*/*Vs* zones near subduction interfaces in Nicoya and other subduction zones (Audet & Kim, 2016; Audet & Schwartz, 2013; Chaves & Schwartz, 2016). In Nicoya, the high *Vp*/*Vs* structure extends from the deep transition zone to the seismogenic portion, consistent with our constrained low strength on the megathrust. Such tomographic images qualitatively indicate material properties on the megathrust in their observation periods. The megathrust strength may evolve with time due to fluid migration. In the sense of timing, our study quantifies the strength on the megathrust immediately prior to a large earthquake.

Our results are based on the LSW law. Beside the slip-dependent phenomena, friction has been observed to depend on slip velocity (Beeler et al., 2008; Di Toro et al., 2011; Dieterich, 1979). The friction coefficient decreases exponentially with sliding velocity close to the typical seismic slip rate (m/s). Such exponential decay of rate-weakening friction leads to an exponential slip-weakening curve, rather than being linear. It has been found that models using rate-weakening laws do not qualitatively differ with those using the LSW law (Bizzarri et al., 2001; Luo & Duan, 2018). However, friction laws with exponential weakening curves result in a faster energy release at the onset of slip and therefore may produce slightly more energetic rupture fronts than may those based on the LSW law (Dunham, 2007; Luo & Duan, 2018; Ryan & Oglesby, 2014). If we adopt a rate-weakening friction law to reproduce the rupture process of the 2012 Nicoya M_w 7.6 earthquake, a slightly higher yield stress may be inferred.

We here estimate the potential difference from adopting a LSW law by comparing it with rate-weakening laws with an exponential decay (Mizoguchi et al., 2007) and a power law decay (Abercrombie & Rice, 2005; Rice & Uenishi, 2002), which are expressed below, respectively.

$$\tau_f = \begin{cases} \tau_d + (\tau_s - \tau_d)\exp\left(\dfrac{\ln(0.05)\delta}{D_0}\right) & \delta < D_0 \\ \tau_d & \delta \geq D_0 \end{cases} \tag{6}$$

$$\tau_f = \begin{cases} \tau_s - (\tau_s - \tau_d)\left(\dfrac{\delta}{D_0}\right)^p & \delta < D_0 \\ \tau_d & \delta \geq D_0 \end{cases} \tag{7}$$

In the exponential slip-weakening law (Equation 6), D_0 is defined as the critical displacement at which the friction reduces from the peak by 95% of $(\tau_s - \tau_d)$, close to the critical weakening distance in the LSW law. The fracture energies for the two weakening laws at slip greater than D_0 are $G \doteq 0.33\sigma_n(f_s - f_d)D_0$ and $G = \sigma_n(f_s - f_d)D_0 p/(p+1)$, respectively, where p is the power index that is suggested to be 0.2–0.5 from friction experiments and seismic observations (Abercrombie & Rice, 2005; Di Toro et al., 2011). Assuming that fracture energies are well constrained, the product of D_0 and the strength drop may be underestimated by a factor of 1.5–3 by assuming a LSW curve. If we assume the same D_0, the average yield stress should be no more than 23 MPa, still very low for such seismogenic depths.

6. Conclusion

With constraints from dynamic simulations, kinematic models, and near-field observations, we resolve the dynamic rupture process of the 2012 M_w 7.6 Nicoya earthquake and constrain the strength on the Nicoya

megathrust prior to the earthquake. The average strength before the rupture is suggested to be not higher than 7.5 MPa, and the peak strength on the down-dip patch should be less than 18 MPa. We attribute such low strength to the near-lithostatic pore pressure, which is implied by seismic studies in the region (Audet & Schwartz, 2013; Chaves & Schwartz, 2016). Our estimated strength on the megathrust can serve as a reference for parameter prescriptions in numerical simulations for future seismic hazard assessments and can advance our understanding of the dynamics of subduction systems.

Data Availability Statement

The data sets used in this study contain high-rate, low-rate GPS data and strong motion data. The time series of GPS data can be downloaded from UNAVCO (https://www.unavco.org/data/gps-gnss/gps-gnss.html). The strong motion data can be downloaded from LIS-UCR (http://www.lis.ucr.ac.cr). We obtain three-component ground displacement data of the high-rate GPS from Yin and Wdowinski (2014). We transform the time series of displacement on high-rate GPS into velocity waveforms. Solutions of static offsets of high- and low-rate GPS measurements are from Protti et al. (2014). We integrate the acceleration data on strong motion stations to obtained velocity waveforms. The final slip distribution and slip rate history on the fault in our preferred dynamic rupture model are available at 10.4121/uuid:307369d2-778d-4ede-a733-cd38f3ff0c6a.

Acknowledgments

This study is supported by the Hong Kong Research Grants Council (grants 14313816, 14306418, and 14306119); CUHK Direct Grant from the Faculty of Science; China Earthquake Science Experiment Project, CEA (grants 2017CESE0103 and 2018CSES0102); and State Key Lab of Earthquake Dynamics (grant LED2017B07), Institute of Geology, CEA. We benefit from discussion with Dr. Huihui Weng in Nice University.

References

Aagaard, B. T., Knepley, M. G., & Williams, C. A. (2013). A domain decomposition approach to implementing fault slip in finite-element models of quasi-static and dynamic crustal deformation. *Journal of Geophysical Research: Solid Earth*, *118*, 3059–3079. https://doi.org/10.1002/jgrb.50217

Abercrombie, R. E., & Rice, J. R. (2005). Can observations of earthquake scaling constrain slip weakening? *Geophysical Journal International*, *162*, 406–424. https://doi.org/10.1111/j.1365-246X.2005.02579.x

Audet, P., & Kim, Y.-H. (2016). Teleseismic constraints on the geological environment of deep episodic slow earthquakes in subduction zone forearcs: A review. *Tectonophysics*, *670*, 1–15. https://doi.org/10.1016/j.tecto.2016.01.005

Audet, P., & Schwartz, S. Y. (2013). Hydrologic control of forearc strength and seismicity in the Costa Rican subduction zone. *Nature Geoscience*, *6*(10), 852–855. https://doi.org/10.1038/ngeo1927

Beeler, N. M., Tullis, T. E., & Goldsby, D. L. (2008). Constitutive relationships and physical basis of fault strength due to flash heating. *Journal of Geophysical Research*, *113*, B01401. https://doi.org/10.1029/2007JB004988

Bizzarri, A., Cocco, M., Andrews, D. J., & Boschi, E. (2001). Solving the dynamic rupture problem with different numerical approaches and constitutive laws. *Geophysical Journal International*, *144*(3), 656–678. https://doi.org/10.1046/j.1365-246x.2001.01363.x

Byerlee, J. (1978). Friction of rocks. *Pure and Applied Geophysics*, *116*(4-5), 615–626. https://doi.org/10.1007/BF00876528

Carpenter, B. M., Marone, C., & Saffer, D. M. (2011). Weakness of the San Andreas Fault revealed by samples from the active fault zone. *Nature Geoscience*, *4*(4), 251–254. https://doi.org/10.1038/ngeo1089

Chaves, E. J., & Schwartz, S. Y. (2016). Monitoring transient changes within overpressured regions of subduction zones using ambient seismic noise. *Science Advances*, *2*, e1501289. https://doi.org/10.1126/sciadv.1501289

Christeson, G. L., McIntosh, K. D., Shipley, T. H., Flueh, E. R., & Goedde, H. (1999). Structure of the Costa Rica convergent margin, offshore Nicoya Peninsula. *Journal of Geophysical Research*, *104*(B11), 25,443–25,468. https://doi.org/10.1029/1999JB900251

Day, S. M., Dalguer, L. A., Lapusta, N., & Liu, Y. (2005). Comparison of finite difference and boundary integral solutions to three-dimensional spontaneous rupture. *Journal of Geophysical Research*, *110*, B12307. https://doi.org/10.1029/2005JB003813

De Paola, N., Hirose, T., Mitchell, T., Di Toro, G., Viti, C., & Shimamoto, T. (2011). Fault lubrication and earthquake propagation in thermally unstable rocks. *Geology*, *39*(1), 35–38. https://doi.org/10.1130/G31398.1

DeMets, C., Gordon, R. G., & Argus, D. F. (2010). Geologically current plate motions. *Geophysical Journal International*, *181*(1), 1–80. https://doi.org/10.1111/j.1365-246X.2009.04491.x

Di Toro, G., Han, R., Hirose, T., De Paola, N., Nielsen, S., Mizoguchi, K., et al. (2011). Fault lubrication during earthquakes. *Nature*, *471*(7339), 494–498. https://doi.org/10.1038/nature09838

Dieterich, J. H. (1979). Modeling of rock friction: 1. Experimental results and constitutive equations. *Journal of Geophysical Research*, *84*(B5), 2161–2168. https://doi.org/10.1029/JB084iB05p02161

Dixon, T. H., Jiang, Y., Malservisi, R., McCaffrey, R., Voss, N., Protti, M., & Gonzalez, V. (2014). Earthquake and tsunami forecasts: Relation of slow slip events to subsequent earthquake rupture. *Proceedings of the National Academy of Sciences of the United States of America*, *111*(48), 17,039–17,044. https://doi.org/10.1073/pnas.1412299111

Dunham, E. M. (2007). Conditions governing the occurrence of supershear ruptures under slip-weakening friction. *Journal of Geophysical Research*, *112*, B07302. https://doi.org/10.1029/2006JB004717

Fulton, P., Brodsky, E., Kano, Y., Mori, J., Chester, F., Ishikawa, T., et al. (2013). Low coseismic friction on the Tohoku-Oki fault determined from temperature measurements. *Science*, *342*(6163), 1214–1217. https://doi.org/10.1126/science.1243641

Gallovič, F., Valentová, Ľ., Ampuero, J.-P., & Gabriel, A.-A. (2019). Bayesian dynamic finite-fault inversion: 2. Application to the 2016 M_w 6.2 Amatrice, Italy, earthquake. *Journal of Geophysical Research: Solid Earth*, *124*, 6970–6988. https://doi.org/10.1029/2019JB017512

Gao, X., & Wang, K. (2014). Strength of stick-slip and creeping subduction megathrusts from heat flow observations. *Science*, *345*(6200), 1038–1041. https://doi.org/10.1126/science.1255487

Guatteri, M., & Spudich, P. (2000). What can strong-motion data tell us about slip-weakening fault-friction laws? *Bulletin of the Seismological Society of America*, *90*(1), 98–116. https://doi.org/10.1785/0119990053

Han, R., Shimamoto, T., Hirose, T., Ree, J.-H., & Ando, J. (2007). Ultralow friction of carbonate faults caused by thermal decomposition. *Science*, *316*(5826), 878–881. https://doi.org/10.1126/science.1139763

Hardebeck, J. L. (2012). Coseismic and postseismic stress rotations due to great subduction zone earthquakes. *Geophysical Research Letters*, *39*, L21313. https://doi.org/10.1029/2012GL053438

Hardebeck, J. L. (2015). Stress orientations in subduction zones and the strength of subduction megathrust faults. *Science*, *349*(6253), 1213–1216. https://doi.org/10.1126/science.aac5625

Harris, R. (2004). Numerical simulations of large earthquakes: Dynamic rupture propagation on heterogeneous faults. *Pure and Applied Geophysics*, *161*, 2171–2181. https://doi.org/10.1007/s00024-004-2556-8

Ida, Y. (1972). Cohesive force across the tip of a longitudinal-shear crack and Griffith's specific surface energy. *Journal of Geophysical Research*, *77*(20), 3796–3805. https://doi.org/10.1029/JB077i020p03796

Kano, Y., Mori, J., Fujio, R., Ito, H., Yanagidani, T., Nakao, S., & Ma, K. F. (2006). Heat signature on the Chelungpu fault associated with the 1999 Chi-Chi, Taiwan earthquake. *Geophysical Research Letters*, *33*, L14306. https://doi.org/10.1029/2006GL026733

Kato, N. (2012). Dependence of earthquake stress drop on critical slip-weakening distance. *Journal of Geophysical Research*, *117*, B01301. https://doi.org/10.1029/2011JB008359

Kuo, L.-W., Li, H., Smith, S. A. F., Di Toro, G., Suppe, J., Song, S.-R., et al. (2013). Gouge graphitization and dynamic fault weakening during the 2008 Mw 7.9 Wenchuan earthquake. *Geology*, *42*(1), 47–50. https://doi.org/10.1130/g34862.1

Lachenbruch, A. H., & Sass, J. H. (1980). Heat flow and energetics of the San Andreas Fault zone. *Journal of Geophysical Research*, *85*(B11), 6185–6222. https://doi.org/10.1029/JB085iB11p06185

Lamb, S. (2006). Shear stresses on megathrusts: Implications for mountain building behind subduction zones. *Journal of Geophysical Research*, *111*, B07401. https://doi.org/10.1029/2005JB003916

Li, D., McGuire, J. J., Liu, Y., & Hardebeck, J. L. (2018). Stress rotation across the Cascadia megathrust requires a weak subduction plate boundary at seismogenic depths. *Earth and Planetary Science Letters*, *485*, 55–64. https://doi.org/10.1016/j.epsl.2018.01.002

Li, H., Xue, L., Brodsky, E., Mori, J., & Fulton, P. (2015). Long-term temperature records following the M_w 7.9 Wenchuan (China) earthquake consistent with low friction. *Geology*, *43*(2), 163–166. https://doi.org/10.1130/G35515.1

Liu, C., Zheng, Y., Xiong, X., Wang, R., López, A., & Li, J. (2015). Rupture processes of the 2012 September 5 M_w7.6 Nicoya, Costa Rica earthquake constrained by improved geodetic and seismological observations. *Geophysical Journal International*, *203*(1), 175–183. https://doi.org/10.1093/gji/ggv295

Liu, Y., & Rice, J. R. (2007). Spontaneous and triggered aseismic deformation transients in a subduction fault model. *Journal of Geophysical Research*, *112*, B09404. https://doi.org/10.1029/2007JB004930

Lockner, D. A., Morrow, C., Moore, D., & Hickman, S. (2011). Low strength of deep San Andreas fault gouge from SAFOD core. *Nature*, *472*(7341), 82–85. https://doi.org/10.1038/nature09927

Luo, B., & Duan, B. (2018). Dynamics of nonplanar thrust faults governed by various friction laws. *Journal of Geophysical Research: Solid Earth*, *123*, 5147–5168. https://doi.org/10.1029/2017JB015320

Ma, S., Custodio, S., Archuleta, R. J., & Liu, P. (2008). Dynamic modeling of the 2004 M_w 6.0 Parkfield, California, earthquake. *Journal of Geophysical Research*, *113*, B02301. https://doi.org/10.1029/2007JB005216

Matsuzawa, T., Hirose, H., Shibazaki, B., & Obara, K. (2010). Modeling short- and long-term slow slip events in the seismic cycles of large subduction earthquakes. *Journal of Geophysical Research*, *115*, B12301. https://doi.org/10.1029/2010JB007566

Mizoguchi, K., Hirose, T., Shimamoto, T., & Fukuyama, E. (2007). Reconstruction of seismic faulting by high-velocity friction experiments: An example of the 1995 Kobe earthquake. *Geophysical Research Letters*, *34*, L01308. https://doi.org/10.1029/2006GL027931

Noda, H., & Shimamoto, T. (2005). Thermal pressurization and slip-weakening distance of a fault: An example of the Hanaore fault, southwest Japan. *Bulletin of the Seismological Society of America*, *95*, 1224–1233. https://doi.org/10.1785/0120040089

Protti, M., González, V., Newman, A. V., Dixon, T. H., Schwartz, S. Y., Marshall, J. S., et al. (2014). Nicoya earthquake rupture anticipated by geodetic measurement of the locked plate interface. *Nature Geoscience*, *7*(2), 117–121. https://doi.org/10.1038/ngeo2038

Protti, M., Güendel, F., & Malavassi, E. (2001). *Evaluación del potencialsísmico de laPenínsula de Nicoya*, (p. 144). Costa Rica, Editorial Fundación UNA: Heredia.

Rice, J. R. (2006). Heating and weakening of faults during earthquake slip. *Journal of Geophysical Research*, *111*, B05311. https://doi.org/10.1029/2005JB004006

Rice, J. R., Uenishi, K. (2002), Slip development and instability on a heterogeneously loaded fault with power-law slip-weakening, *Eos, Transactions American Geophysical Union, Fall Meeting Suppl.*, *83*(47), Abstract S61E-06.

Ryan, K. J., & Oglesby, D. D. (2014). Dynamically modeling fault step overs using various friction laws. *Journal of Geophysical Research: Solid Earth*, *119*, 5814–5829. https://doi.org/10.1002/2014JB011151

Seno, T. (2009). Determination of the pore fluid pressure ratio at seismogenic megathrusts in subduction zones: Implications for strength of asperities and Andean-type mountain building. *Journal of Geophysical Research*, *114*, B05405. https://doi.org/10.1029/2008JB005889

Tanikawa, W., & Shimamoto, T. (2009). Frictional and transport properties of the Chelungpu fault from shallow borehole data and their correlation with seismic behavior during the 1999 Chi-Chi earthquake. *Journal of Geophysical Research*, *114*, B01402. https://doi.org/10.1029/2008JB005750

Ujiie, K., Tanaka, H., Saito, T., Tsutsumi, A., Mori, J., Kameda, J., et al. (2013). Low coseismic shear stress on the Tohoku-Oki megathrust determined from laboratory experiments. *Science*, *342*(6163), 1211–1214. https://doi.org/10.1126/science.1243485

Viesca, R. C., & Garagash, D. I. (2015). Ubiquitous weakening of faults due to thermal pressurization. *Nature Geoscience*, *8*(11), 875–879. https://doi.org/10.1038/ngeo2554

Violay, M., Di Toro, G., Nielsen, S., Spagnuolo, E., & Burg, J. (2015). Thermo-mechanical pressurization of experimental faults in cohesive rocks during seismic slip. *Earth and Planetary Science Letters*, *429*, 1–10. https://doi.org/10.1016/j.epsl.2015.07.054

Walter, J. I., Schwartz, S. Y., Protti, J. M., & Gonzalez, V. (2011). Persistent tremor within the northern Costa Rica seismogenic zone. *Geophysical Research Letters*, *38*, L01307. https://doi.org/10.1029/2010GL045586

Weng, H., Huang, J., & Yang, H. (2015). Barrier-induced supershear ruptures on a slip-weakening fault. *Geophysical Research Letters*, *42*, 4824–4832. https://doi.org/10.1002/2015GL064281

Weng, H., & Yang, H. (2017). Seismogenic width controls aspect ratios of earthquake ruptures. *Geophysical Research Letters*, *44*, 2725–2732. https://doi.org/10.1002/2016GL072168

Weng, H., & Yang, H. (2018). Constraining frictional properties on fault by dynamic rupture simulations and near-field observations. *Journal of Geophysical Research: Solid Earth*, *123*, 6658–6670. https://doi.org/10.1029/2017JB015414

Yang, H., Liu, Y., & Lin, J. (2012). Effects of subducted seamount on megathrust earthquake nucleation and rupture propagation. *Geophysical Research Letters*, *39*, L24302. https://doi.org/10.1029/2012GL053892

Yang, H., Yao, S., He, B., Newman, A. V., & Weng, H. (2019). Deriving rupture scenarios from interseismic locking distributions along the subduction megathrust. *Journal of Geophysical Research: Solid Earth*, *124*, 10,376–10,392. https://doi.org/10.1029/2019JB017541

Yao, L., Ma, S., Shimamoto, T., & Togo, T. (2013). Structures and high velocity frictional properties of the Pingxi fault zone in the Longmenshan fault system, Sichuan, China, activated during the 2008 Wenchuan earthquake. *Tectonophysics*, *599*, 135–156. https://doi.org/10.1016/j.tecto.2013.04.011

Yin, H., & Wdowinski, S. (2014). Improved detection of earthquake-induced ground motion with spatial filter: Case study of the 2012 M = 7.6 Costa Rica earthquake. *GPS Solutions*, *18*(4), 563–570. https://doi.org/10.1007/s10291-013-0353-5

Yue, H., Lay, T., Schwartz, S. Y., Rivera, L., Protti, M., Dixon, T. H., et al. (2013). The 5 September 2012 Nicoya, Costa Rica M_w 7.6 earthquake rupture process from joint inversion of high-rate GPS, strong-motion, and teleseismic P wave data and its relationship to adjacent plate boundary interface properties. *Journal of Geophysical Research: Solid Earth*, *118*, 5453–5466. https://doi.org/10.1002/jgrb.50379